Selective catalytic oxidation of ammonia over different topologies nano Cu/zeolites

Hao Wang,[1] Runduo Zhang,[1,*] Yiyun Liu,[2] Peixin Li,[1] Hongxia Chen,[1] Feng Ryan Wang,[2] Wey Yang Teoh[3,*]

[1]State Key Laboratory of Chemical Resource Engineering, Beijing Key Laboratory of Energy Environmental Catalysis, Beijing University of Chemical Technology, 100029 P. R. China

[2]Department of Chemical Engineering, University College London, Torrington Place, London WC1E 7JE, United Kingdom

[3]School of Chemical Engineering, The University of New South Wales, Sydney, NSW 2052, Australia

*Corresponding author: R. Zhang (zhangrd@mail.buct.edu.cn);
W. Y. Teoh (wyteoh@unsw.edu.au)

Abstract

The selective catalytic oxidation of ammonia (NH_3-SCO) is the last mitigation step in the exhaust treatment by a 4-way catalytic converter to convert any excess and unreacted NH_3 (that was used as a reductant of NO_x) to the environmentally benign N_2 and H_2O. Here, we report a series of highly reactive and selective nano Cu/zeolites for the NH_3-SCO reaction. The NH_3-SCO activity was found in the order of nano Cu/ZSM-5 (MFI topology) > Cu/Beta (BEA) > Cu/MCM-49 (MWW) > Cu/Y (FAU) > Cu/Mordenite (MOR) > Cu/Ferrierite (FER). The best catalyst, i.e., nano Cu/ZSM-5, achieves 98% NH_3 conversion at 250 °C with N_2 yield maintained at > 98% even at up 500 °C. When assessed under practical exhaust conditions in the presence of moisture (5% H_2O) as well as that after hydrothermal aging (5% H_2O, 850 °C, 8 h), the nano Cu/ZSM-5 exhibited only minor deactivation as a result of its good retainment of Cu dispersion, pore structure and specific surface area. Furthermore, small micropore (10-membered ring, 10-MR) topologies were found to be crucial in maintaining high N_2 yield. For Cu/Y and Cu/Mordenite, which composed of 12-MR pores that are non-interconnected with smaller pores, their N_2 yields were compromised by forming NO_x at temperatures above 400 °C. Based on the *in situ* DRIFT study, the iSCR mechanism appears to be applicable for all fresh and aged Cu/zeolites in the exception of fresh Cu/MCM-49 that follows the imide mechanism.

Keywords: Ammonia; selective catalytic oxidation (SCO); isolated copper; micropores; hydrothermal aging

1. Introduction

The increasingly stringent environmental emission standards are placing immense stress on stationary (e.g., incinerators and thermal power plants) and mobile (e.g., diesel vehicles) combustion-related processes. For example, the Euro VI standard for diesel passenger cars that limit emissions to no more than 80 mg km^{-1} of NO_x, 17 mg km^{-1} of cumulative of hydrocarbons and NO_x and 4.5 mg km^{-1} of particulate matter is so difficult to meet that it inadvertently led to the "Dieselgate" scandal. Likewise, the new NO_x emission standards for coal-fired power plant are limited to 50, 95.3, 150 and 200 μg m^{-3} in China, USA, Europe and Japan, respectively. In these cases, both mobile and stationary sources, the selective catalytic reduction of NO_x (NH_3-SCR) appears to be the leading solution for the abatement of NO_x, where urea solution (which thermally decomposes to NH_3) is injected directly into the exhaust to reduce NO_x to N_2 and H_2O.[1,2] For automobile applications, this is carried out in the 4-way catalytic converter. A major setback that plagues the NH_3-SCR is the so-called ammonia slip problem, where excess or unreacted ammonia escapes through the exhausts. To limit NH_3 slip, the current practice is to introduce 5-10% less stoichiometric amount of NH_3 than that required for a full reduction of NO_x, which means that some NO_x emissions would be inevitable. With increasingly stringent NO_x emission standards being put in place, such practice will eventually be curbed, necessitating closer to stoichiometric or excess amount of NH_3 reductant be injected.

As the applications of NH_3-SCR toward achieving minimum NO_x emissions become more prominent, so would the accompanying technology to mitigate the NH_3 slip problem in face of its toxicity, strong odour and corrosive nature.[3] Different methods have been proposed for the removal of ammonia that include biological, chemical and physical means, some of which are slow-response while others may require neutralization or regeneration of the capturing medium.[4] To cope with the fast dynamic of the NH_3-SCR cycles especially in the automobile applications, the selective catalytic oxidation of ammonia (NH_3-SCO) to benign N_2 and H_2O (Eq. 1) is considered the most ideal mitigation technology:

$$2NH_3 + 1.5O_2 \rightarrow N_2 + 3H_2O \qquad \text{(Eq. 1)}$$

The portable ammonia slip catalytic unit, which is placed at the outlet of the 4-way catalytic converter, serves as the final exhaust treatment prior to discharge into the atmosphere. In that

sense, it is essential that the NH_3-SCO does not overly oxidize the NH_3 back to NO_x. A high N_2 selectivity is of utmost importance and is an emerging topic as summarized below.[5]

Noble metal-based catalysts (e.g., Pt, Ir and Au) are known to be active for NH_3 oxidation at low temperatures (< 300 °C); however, the level of N_2 selectivity was unsatisfactory for the reason that the main byproduct at the high-temperature region was N_2O.[6-8] Such is the case of overly oxidative catalysts. He *et al*.[4,9] reported that Cu-Ag/Al_2O_3 displays a relatively low temperature (< 320 °C) oxidation of NH_3 with excellent N_2 selectivity (> 95%). With trends directed toward the use of non-precious metals, researchers have studied the NH_3-SCO over transition metal (Ni, Fe, Mn, and Cu) oxides supported on γ-Al_2O_3,[10,11] mixed metal oxides of hydrotalcite,[12] spinel,[13] and perovskite structures, as well as ion-exchanged zeolites.[14,15] Among them, Chmielarz *et al*.[12] identified the presence of copper oxide species on Cu-Mg-Al oxide as the active sites for NH_3-SCO, achieving complete conversion at 425 °C and N_2 selectivity above 90%. The temperature for complete conversion of NH_3 can be lowered to 250 °C when catalyzed over highly dispersed CuO on CeO_2 as a result of the swift surface redox from Ce^{4+}–O^{2-}–Cu^{2+} to Ce^{3+}–□–Cu^{+}.[16] As for zeolite-based catalysts, Long and Yang[17] investigated a series of transition metal (Cr, Mn, Fe, Co, Ni, Cu) ion-exchanged ZSM-5 (MFI topology) and found that iron and copper ion-exchanged ZSM-5 could achieve nearly 100% NH_3 conversion to N_2 at 450 °C. When supported on Y zeolites (FAU topology),[18,19] the NH_3-SCO activity of the metals follows the trend: Cu-Y > Cr-Y > Ag-Y > Co-Y > Fe-Y > Ni-Y ≈ Mn-Y.[20] Yang and coworkers[15,21] reported the beneficial effects of the variable valency of active metal cations on ZSM-5 that led to the enhanced oxygen adsorption and activation during the NH_3-SCO reaction.

In this paper, we demonstrate the efficacy of Cu/zeolites and the importance of different microporous topologies (i.e., pore size and structure) on their performance of NH_3-SCO. To do so, we varied the topologies of the zeolites (ZSM-5, Beta, Y, Ferrierite, Mordenite, MCM-49). For practical relevance, we carried out the assessments under practical reaction conditions as well as that after accelerated hydrothermal aging. To the best of our knowledge, the work is the first to establish the importance of the combination of highly dispersed Cu species and narrow zeolite pores that in turn govern the high activity and N_2 selectivity, respectively.

2. Experimental

2.1 Synthesis of Cu/zeolites

Commercial zeolites, H-Mordenite (Si/Al = 10, MOR topology), H-MCM-49 (Si/Al = 12, MMW topology) and H-Ferrierite (Si/Al = 15, FER topology) were obtained from Shanghai Novel Chemical Technology Co., Ltd, while H-Beta (Si/Al = 15, BEA topology) and H-Y (Si/Al = 15) were obtained from Nankai Catalyst Company. ZSM-5 (Si/Al = 13, MFI topology) was synthesized using the hydrothermal method (Please see the Supporting Information for detailed synthesis). The zeolites were impregnated with 0.2 M of aqueous-dissolved $Cu(NO_3)_2 \cdot 3H_2O$ (≥99.0 %, Aladdin) to a nominal metal loading of 3 wt.%. The impregnated zeolites were transferred a vacuum evaporator at 80 °C for 30 minutes to remove the moisture, before being further dried in a convection oven at 100 °C for 6 h. The dried zeolites were calcined in a muffle furnace at 550 °C for 8 h. The as-prepared Cu/zeolites were pelletized and sieved using 40-60 meshes.

2.2 Characterization of Cu/zeolites

The crystallographic structure of the Cu/zeolites was confirmed by X-ray diffraction (XRD), using the Bruker D5005 diffractometer and Cu *K*α (λ = 1.5406 Å) as the radiation source. The XRD spectra were measured in range of 2θ = 5-60°, and the crystal phases were matched to the JCPDS references. The specific surface area (SSA) was measured by N_2 adsorption at 77 K on MicroActive ASAP 2460 using the Brunauer-Emmett-Teller (BET) method. The Cu/zeolites were imaged by scanning electron microscopy (SEM) with a Supra microscope (Carl Zeiss). X-ray photoelectron spectroscopy (XPS) was conducted on Thermo Fisher ESCALAB 250 under ultrahigh vacuum (UHV) and using monochromatic Al *K*α as the radiation source. The binding energies were calibrated with respect to the C 1s energy of incidental C–C bond at 285.0 eV. Because of the close proximity of Cu^{2+} and Cu^{+} binding energies, the former was distinguished and quantified using its unique satellite peak areas (I_{sat}), where the $I_{Cu^{2+}} : I_{sat} = 1.89$.[22] The dispersion of surface copper was determined by dissociative N_2O adsorption at 50 °C using the procedure described in literature.[23] The electron paramagnetic resonance (EPR) measurements were recorded on Bruker A300 X-band

spectrometer and the signals of isolated Cu^{2+} were collected in the region from 2250 to 4250 G at 155 K. Prior to the EPR analysis, each sample was evacuated at room temperature for 1 h.

Temperature programmed reduction by hydrogen (H_2-TPR) was carried out inside a fixed-bed reactor with sample (~200 mg) pretreated *in situ* by 20 ml min^{-1} O_2/He at 500 °C for 30 min. After cooling down to room temperature under the same atmosphere, the sample was exposed to 20 ml min^{-1} of 5% H_2/Ar and heated at a rate of 5 °C min^{-1} from 100 to 800 °C. H_2 consumption was monitored on-line by thermal conductivity detector (TCD) using a flow of 20 ml min^{-1} of 5% H_2/Ar as reference gas. The TCD signal was calibrated using the corresponding standard gases containing known concentrations of the components. Temperature programmed desorption of NH_3 (NH_3-TPD) were performed on GC4000A and the signal was monitored by thermal conductivity detector (TCD). Typically, the samples were pretreated at 500 °C for 1 h under He flow. After the samples cooled down to the room temperature, they were saturated under 4% NH_3/He at 100 °C for 1 h. The samples were then purged with He for 2 h and finally heated to 650 °C at a rate of 10 °C min^{-1}.

In situ DRIFTS were carried out in a Bruker TENSOR 27 FT-IR spectrometer equipped with a gas cell and liquid nitrogen cooled MCT detector. The samples were pretreated at 300 °C for 4 h to eliminate physically adsorbed gases and water. Before recording the spectra, the sample was exposed to 20 ml min^{-1} He for 30 min to collect the background signal, and then exposed to the feed gas at the desired temperature. Each spectrum was collected with a resolution of 2 cm^{-1} and an accumulation of 32 scans.

2.3 Assessments of NH_3-SCO

The catalytic assessments were performed in a quartz fixed-bed reactor (3 cm i.d.) loaded with ~200 mg catalyst by flowing 350 ml min^{-1} (corresponding to a space velocity of approximate 45,000 h^{-1}) of reactant gas comprising of 1000 ppm NH_3, 10% O_2, and with or without 5% H_2O with the balance of He. Prior to the reaction, each catalyst sample was purged with 30 ml min^{-1} He for 1 h at the designated reaction temperature. A thermocouple was inserted into centre of the catalyst bed and connected to the temperature controller of the reactor

furnace. The effluent gases (NH_3, N_2O, NO, and NO_2) were monitored using an infrared gas analyzer (Nicolet Nexus 670) equipped with a 2.4 m long-path gas cell. TQ analysis software was used to analyze the IR spectra. For hydrothermal aging, the as-prepared catalysts were exposed to 130 ml min^{-1} of wet air (5% H_2O) at 850 °C (ramp rate of 10 °C min^{-1}) for 8 h, followed by cooling to room temperature under flowing dry air. The catalysts were treated the same as the as-prepared catalysts for the catalytic assessments.

3. Results and Discussion

3.1. Physicochemical characterization of Cu/zeolites

Cu/zeolites (Si/Al ratios = 10-15, Table 1) with different topologies belonging to that of ZSM-5 (MFI topology), Beta (BEA), Zeolite Y (FAU), Mordenite (MOR), Ferrierite (FER), and MCM-49 (MWW) catalysts were characterized by XRD. As can be readily observed from Fig. 1, the XRD patterns of the Cu/zeolites retain the signature diffraction peaks of the native zeolites, which are in turn unique to their specific topologies (Fig. S1).[24-29] In other words, the results confirm the stability of the microporous structures during the Cu impregnation procedure. Minor diffraction lines corresponding to CuO (JCPDS 45-0937) could be detected at $2\theta = 35.5$ and 38.7° in Cu/Y due to the formation of CuO nanoparticles ($d_{XRD} \sim 2.5$ nm), but the peaks were essentially absent in the other Cu/zeolites, inferring the high dispersibility of the Cu species, e.g., isolated Cu^{2+} and Cu^{+}, and/or the formation of small CuO clusters that are invisible under the XRD (Fig. 1, inset). The observation of undisrupted topologies is further confirmed by the almost unchanged pore size distributions of the Cu/zeolites compared with their respective pristine zeolites (Fig. 2). The specific surface area (SSA) of the Cu/zeolites follows the trend of Cu/Y (464 m^2 g^{-1}) > Cu/Beta (319 m^2 g^{-1}) > Cu/ZSM-5 (291 m^2 g^{-1}) > Cu/MCM-49 (270 m^2 g^{-1}) > Cu/Ferrierite (217 m^2 g^{-1}) > Cu/Mordenite (136 m^2 g^{-1}), which represents no more than 15% loss compared to the pristine zeolites. The actual Cu loadings on all Cu/zeolites were confirmed by XRF to closely match the nominal loadings of 3 wt.% (Table 1).

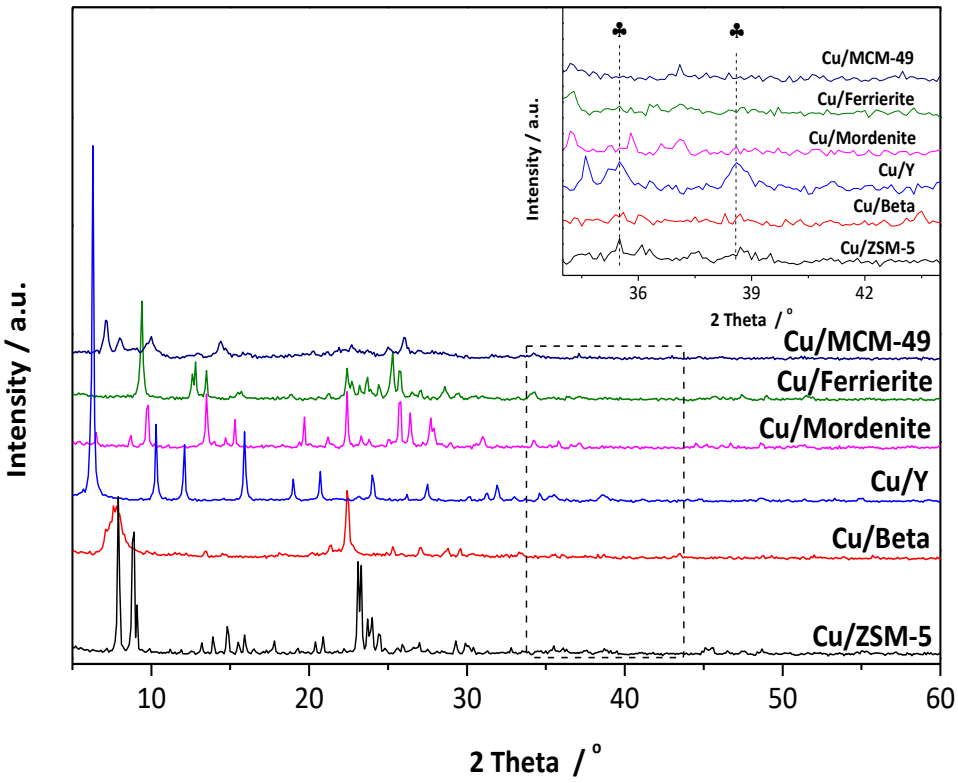

Fig. 1. XRD spectra of Cu ion-exchanged zeolites (ZSM-5, Beta, Y, Mordenite, Ferrierite, and MCM-49) and (inset) the enlarged window at 2 Theta = 35-44°, ♣: Copper oxide (ICSD 45-0937).

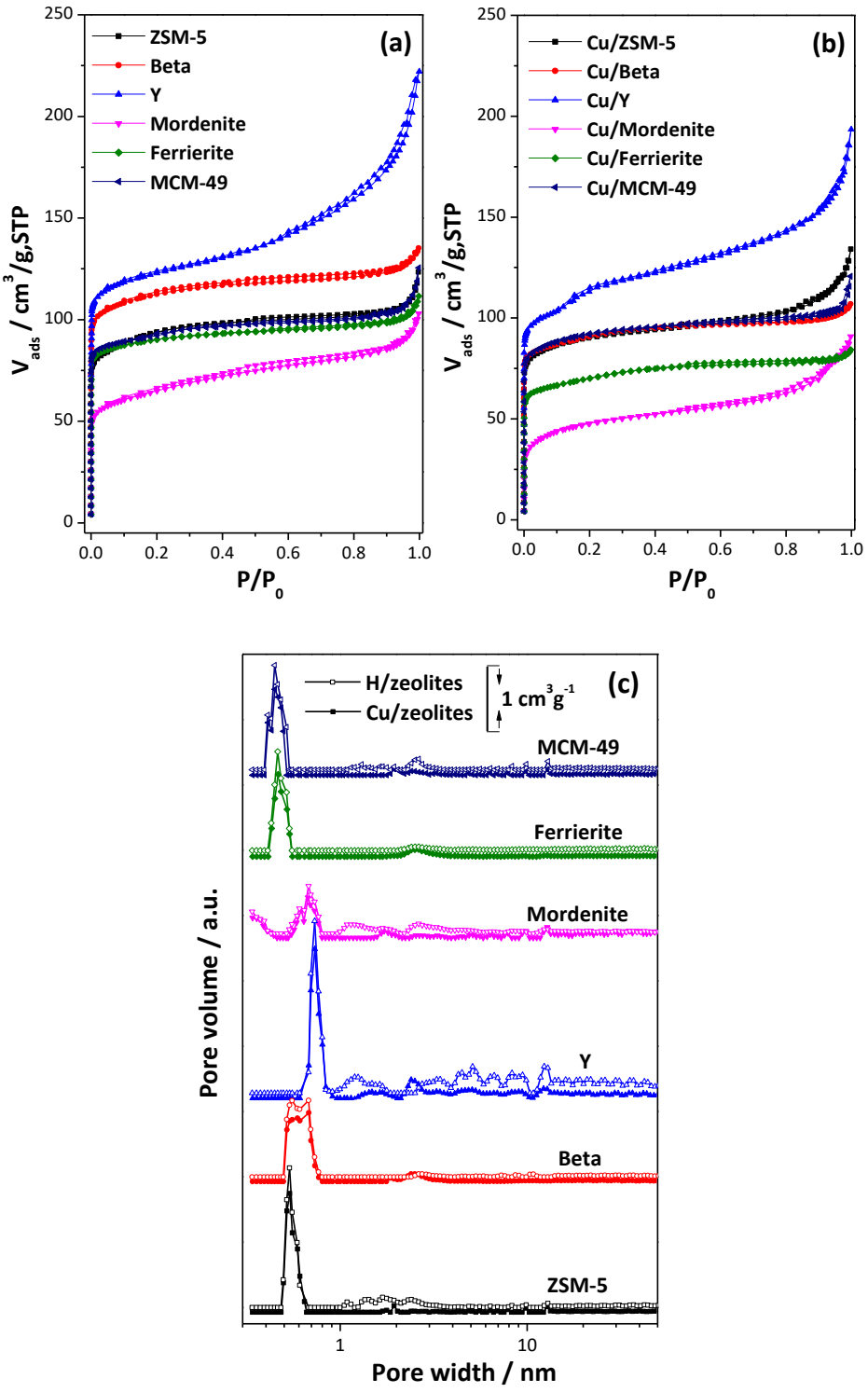

Fig. 2. N_2 adsorption/desorption isotherms (a) before and (b) after Cu loading; (c) Pore size distribution of different zeolites before (open symbol) and after Cu loading (solid symbol).

Table 1. Framework type, specific surface area, Si/Al ratio, Cu loading, and pore channel size of the as-prepared Cu/zeolites as well as those without Cu.

Catalyst	Framework Type Code	SSA (m^2 g^{-1})	Si/Al (mol mol^{-1})[a]	Cu loading (wt.%)[a]	Channel dimension (Å)
ZSM-5	MFI	328	13	-	10-MR (5.1×5.5); 10-MR (5.3×5.6)
Cu/ZSM-5		291		2.95%	
Beta	BEA	436	15	-	12-MR (6.6×6.7); 12-MR (5.6×5.6)
Cu/Beta		319		2.93%	
Y	FAU	514	15	-	12-MR (7.4×7.4)
Cu/Y		464		2.96%	
Mordenite	MOR	233	10	-	12-MR (6.6×7.0); 8-MR (2.6×5.7)
Cu/Mordenite		136		3.06%	
Ferrierite	FER	321	15	-	10-MR (4.2×5.4); 8-MR (3.5×4.8)
Cu/Ferrierite		217		3.10%	
MCM-49	MWW	330	12	-	10-MR (4.0×5.5); 10-MR (4.1×5.1)
Cu/MCM-49		270		3.04%	

[a] Compositions were determined by X-ray fluorescence

The EPR was used to probe the coordination of the Cu^{2+} ions on the zeolite.[30-32] As shown in Fig. 3, the EPR spectra of the Cu/zeolites are characterized by the different intensities and splitting of peaks at high field. The highest signal intensity in Cu/Mordenite indicates the largest amount of isolated Cu^{2+} ions[33] followed by Cu/Y, Cu/ZSM-5, Cu/Beta, Cu/MCM-49, and Cu/Ferrierite. The exact quantification of the isolated Cu^{2+} by EPR is readily tabulated in Table 2. While the EPR is highly sensitive toward paramagnetic species, i.e., isolated Cu^{2+}, other species that may be present, such as isolated Cu^{+} and CuO, are EPR silent.[34] For that reason, the H_2-TPR was used to complement the analyses of Cu speciation as will be discussed below. Meanwhile, the feature of hyperfine splitting at low field (as evident in Fig. 3) for Cu/Y, Cu/MCM-49 and Cu/Ferrierite is attributed to the coupling between the 3*d* unpaired electron and copper nuclear spin,[35] which also reflects higher copper mobility. The $g_{||} = 2.385$ in all Cu/zeolites is consistent with the isolated Cu^{2+} ions located near 6-MR (membered-ring).[36] Although Cu/ZSM-5 and Cu/Mordenite have different framework structure, the coordination

of the isolated Cu^{2+} is similar, in agreement with the earlier findings that the Cu^{2+} ions are located at the bridging T site in the bent 6-MR.[35] The Cu^{2+} cations are located on a flatter 6-MR of Cu/Beta,[37] while the Cu^{2+} in Cu/Y and Cu/MCM-49 have the same copper coordination and are located on the D6-MR sites.[38] Two types of parallel g values, i.e., $g_{||}$ = 2.385 and $g_{||}$ = 2.322, were observed in Cu/Ferrierite, arising from the Cu^{2+} ions located on the 6-MR as well as that on the non-framework aluminum, respectively.[36] It is interesting to note that the feature at 331 mT is close to the higher intensity signal for Cu/Ferrierite (at 332 mT). While it is very possible that there is another hidden signal in the Cu/MCM-49 spectrum with g value similar to that of the Cu/Ferrierite sample (g ~ 2.322), it is not resolved here due to the overlapping with the broad signal. Nevertheless, compared with the more resolved signal (g ~ 2.385), the smaller g value means a more negative coordination environment such as closer to framework oxygen. The difference between Cu/MCM-49 and Cu/Ferrierite lies in the broad signal from the rotation of the Cu(H_2O) complex. The absence of this signal for Cu/Ferrierite suggests low mobility of the Cu complex possibly because the cage and channel of Ferrierite zeolite are rather small.

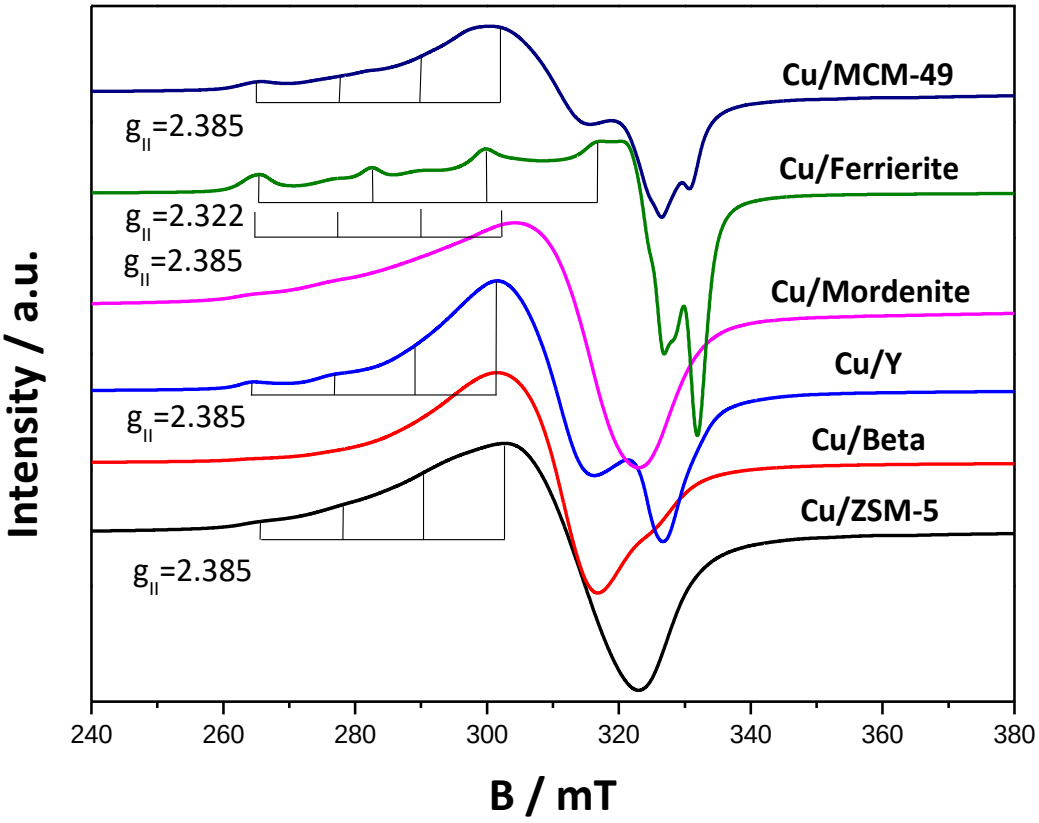

Fig. 3. EPR spectra of different Cu/zeolites measured at 155 K.

The H_2-TPR analysis revealed a more general identification of the Cu speciation, including the non-paramagnetic species not readily identified by EPR. As evident from Fig. 4a, all TPR spectra could be resolved as three Gaussian peaks:[39,40] The first peak, appearing at low temperatures, represents the reduction of isolated Cu^{2+} to Cu^{+} ions;[41] the second peak,[42] appearing at moderate temperatures, corresponds to the reduction of the copper oxide in the zeolites from CuO to Cu^0; and the third peak, appearing at higher temperatures, is assigned to the reduction from Cu^{+} ions to metallic Cu.[41-43] The reducibility of the Cu species could be tuned over a wide range due to their diverse coordination on the zeolite frameworks.[29,44] Integration of the first Gaussian peak quantifies the amount of isolated Cu^{2+} and was found in the following order: Cu/Mordenite > Cu/Y > Cu/ZSM-5 > Cu/Beta > Cu/MCM-49 > Cu/Ferrierite (Table 2). The trend not only concurred with the EPR, but excellent quantitative agreement between the two independent techniques was achieved. This provided a strong verification for the use of H_2-TPR as a reliable tool for analyzing the diverse Cu speciation as well as the quantification of the isolated Cu^{2+} (as credible alternative to EPR).

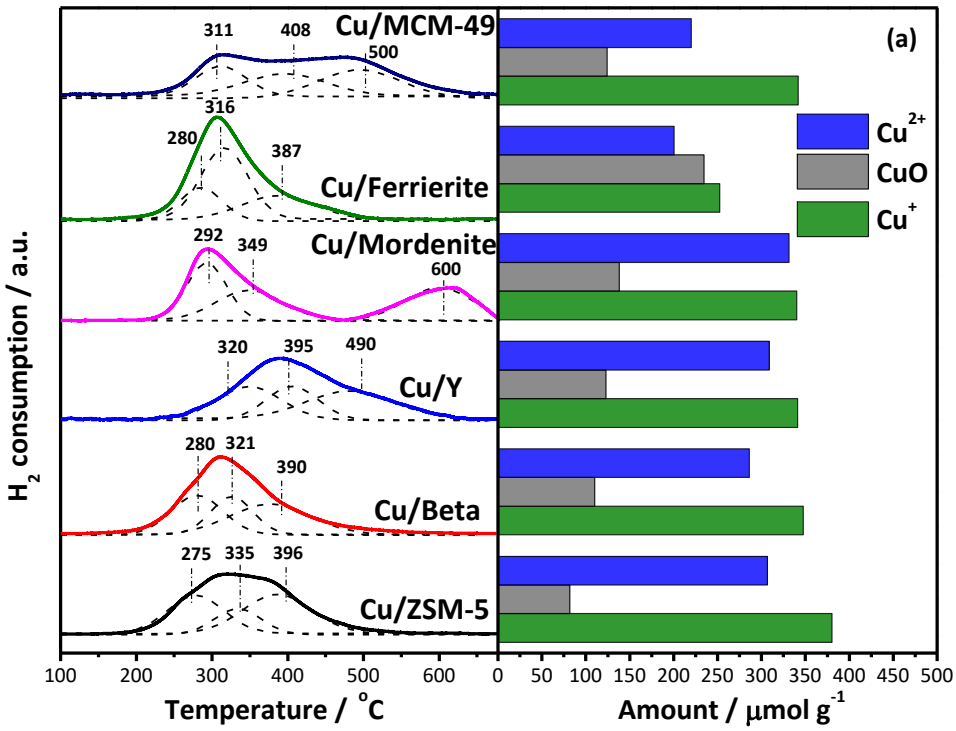

Fig. 4. H_2-TPR profiles of Cu/zeolites (zeolites: ZSM-5, Beta, Y, Mordenite, Ferrierite, MCM-49) as well as the histogram showing the Cu^{2+}, CuO and Cu^{+} as quantified from the low, moderate and high temperature H_2-TPR peaks, respectively.

Table 2. Quantitative analysis of H_2-TPR and EPR on Cu/zeolites (ZSM-5, Beta, Y, Ferrierite, Mordenite, MCM-49).

Catalyst	H_2-TPR peak position (°C)	H_2 consumption (μmol g^{-1})	Total H_2 consumption (μmol g^{-1})	Isolated Cu^{2+} composition, H_2-TPR (μmol g^{-1})[a]	Isolated Cu^{2+} composition, EPR (μmol g^{-1})[b]
Cu/ZSM-5	275	154	426	307	302
	335	82			
	396	190			
Cu/Beta	280	143	427	286	275
	321	110			
	390	174			
Cu/Y	320	155	448	309	311
	395	123			
	490	171			
Cu/Mordenite	292	166	474	332	332
	349	138			
	600	170			
Cu/Ferrierite	280	100	462	201	202
	316	235			
	387	126			
Cu/MCM-49	311	110	406	220	223
	408	125			
	500	171			

[a] Calculated based on the H_2-TPR (Fig. 4)
[b] Calculated based on the EPR (Fig. 3)

As shown in Fig. 4a, despite the sequential reduction of isolated Cu^{2+} to Cu^{+} and further to Cu^{0}, the amount of Cu^{+} measured in the third Gaussian peaks of the Cu/zeolites were not always equal to the corresponding first peaks. This suggests that isolated Cu^{+} coexisted with the surface Cu^{2+} species in the as-prepared catalysts (to be verified by XPS below), and/or that complete reduction of Cu^{2+} (to Cu^{0}) could not proceed completely. It is thus recognized that different zeolites affect the surface distribution of the copper species, which further influenced the redox properties of the catalysts.[45-47] Since the isolated Cu^{2+} in Cu/ZSM-5 is the most easily reduced species (peak reduction temperature at 275 °C), it indicates the highest redox ability followed by Cu/Beta (280 °C), Cu/Ferrierite (280 °C), Cu/Mordenite (292 °C), Cu/MCM-49 (308 °C), and Cu/Y (320 °C).

XPS characterization was carried out to analyze the relative abundance and valence states of the Cu species on the Cu/zeolites surface (Fig. 5a, b and Table 3). The Cu 2*p* binding energy peaks at 952.5±0.2 and 932.4±0.2 eV belong to the Cu $2p_{1/2}$ and $2p_{3/2}$ of Cu^{+}, respectively.[48] Similarly, the binding energy peaks at 953.7±0.2 and 934.2±0.2 eV can be assigned respectively to the Cu $2p_{1/2}$ and $2p_{3/2}$ of Cu^{2+} species (i.e., from both isolated Cu^{2+} and CuO). In addition, the Cu^{2+} satellite peaks can be found at approximately 10 eV higher than the parent Cu^{2+} $2p_{3/2}$ peak.[48] Because of the close proximity between the binding energies of Cu^{+} and Cu^{2+}, direct quantification through peaks deconvolution is subjected to large uncertainties. A more accurate approach that utilizes the calibrated Cu^{2+} satellite peak area is adopted here (see Experimental section for details).[22] Table 3 tabulates the ratios of surface amount of Cu, i.e., n_{Cu2+} and n_{Cu+}, to that of $n_{(Al)}$ from the zeolite supports. The fact that Cu^{2+} coexists with Cu^{+} in all cases of Cu/zeolites corroborates the deduction by H_2-TPR above.

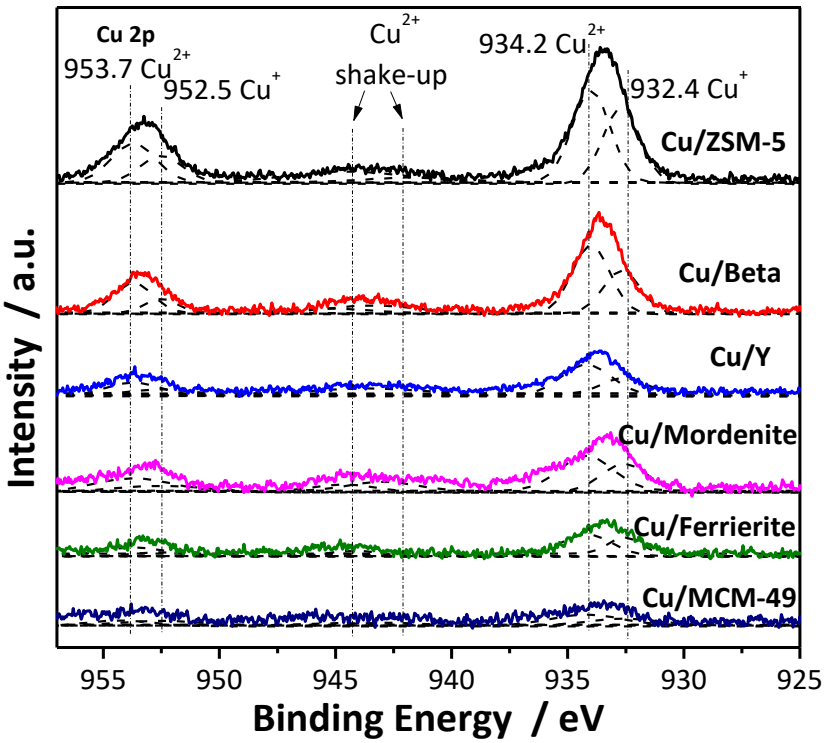

Fig. 5. XPS spectra of Cu2p on Cu/zeolites with different topologies.

Table 3. XPS quantification on the relative surface concentration of the Cu^{2+} and Cu^{+} states with respect to Al on Cu/zeolites.

Catalyst	$n(Cu^{2+})$ /n(Al) (mol mol^{-1})	$n(Cu^{+})$ /n(Al) (mol mol^{-1})
Cu/ZSM-5	0.137	0.104
Cu/Beta	0.131	0.125
Cu/Y	0.116	0.085
Cu/Mordenite	0.124	0.078
Cu/Ferrierite	0.075	0.121
Cu/MCM-49	0.084	0.113

3.2. Selective catalytic oxidation of NH_3 over Cu/zeolites

The Cu/zeolites were assessed for the selective oxidation of NH_3 (1000 ppm) in the presence of 10% O_2. Our strategy is to first assess the catalysts under dry condition, and then moving on to assessing their performances under the more realistic hydrothermal condition (5% H_2O), as well as that after hydrothermal aging. In that way, one can appreciate the influence of the two latter exhaust-practical conditions.

Under the dry feed condition, the most active nano Cu/ZSM-5 shows an onset of NH_3 conversion at ~150°C and reaching complete conversion at 250 °C (Fig. 6a). When represented as half-conversion, the nano Cu/ZSM-5 displays the lowest T_{50} (220 °C), followed by Cu/Beta (257 °C), Cu/MCM-49 (279 °C), Cu/Y (300 °C), Cu/Mordenite (319 °C), and Cu/Ferrierite (344 °C). The trend is in agreement with the Cu dispersion, i.e., amount of surface Cu to that of the bulk, as quantified by the N_2O chemisorption (Table 4). It is worth noting that Cu/Y, despite having the largest specific surface area, shows lower activity than nano Cu/ZSM-5, which can be readily ascribed to the lower Cu dispersion of the former. Although the N_2O chemisorption does not distinguish between isolated Cu ions and surface CuO, additional experiment using CuO control confirms its relatively lower activity (Fig. S4), even when normalized to the surface Cu dispersion. Zhang *et al.*[49] concluded from their studies that the lower activity of CuO may stem from the reduced dispersibility of active sites compared to the isolated Cu ions, and to some extent due to the clogging of micropores. As such, the results

point to the superior active sites of the isolated Cu ions, although the mildly active CuO surface shall not be completely disregarded.

In terms of selectivity, the nano Cu/ZSM-5 attained more than 98% N_2 yield upon reaching its highest conversion at 250 °C and maintaining that at higher temperatures (Fig. 6b). Comparing with some of the best catalysts reported in the literature (Table S1), including those based on precious metals as well as those based on transition metals, the Cu/ZMS-5 is clearly advantageous when considering both activity and selectivity. The Cu/Beta, Cu/MCM-49, and Cu/Ferrierite catalysts, despite being less active than the Cu/ZSM-5, were capable of maintaining >98% N_2 yield upon reaching complete conversions. On the contrary, Cu/Y and Cu/Mordenite were only capable of reaching up to maximum N_2 yields of 89 and 92%, respectively, beyond which N_2 yields drop significantly at the expense of NO_x formation (Fig. S5). It appears that the large 12-MR micropore structures in Cu/Y (3-dimensional FAU, 12-MR pore) and Cu/Mordenite (1-dimensional MOR, 12-MR and 8-MR pores) are limiting the N_2 selectivity. *Note*: See Table 1 on the topologies and aperture dimensions of the different zeolites. While Cu/Beta (3-dimensional BEA, 2 types of 12-MR pores) also comprises of 12-MR pores, its aperture of 5.6 × 5.6 Å is significantly smaller than that of the Cu/Y (7.4 × 7.4 Å) and Cu/Mordenite (6.5 × 7.0 Å), and the fact that the channel pores are interconnected in a 3-dimensional network may have contributed to the high N_2 selectivity. The observation concurs with the report[14] that narrow, channel pores especially those of MFI topology (compared with MOR, FER, BEA, and FAU) are the most favorable for the selective NH_3 conversion to N_2.

Further comparison with Cu/ZSM-5 of different Si/Al ratios found that the current Cu/ZSM-5 (Si/Al = 13) is more active than the Cu/ZSM-5 samples with Si/Al = 53 and 173, as the higher acidity of the former ensures better dispersibility of the isolated Cu^{2+} (Fig. S7). Although Pt (T_{50} = 175 °C), Pd (T_{50} = 175 °C) and Mn/ZSM-5 (T_{50} = 210 °C) display higher activity than Cu/ZSM-5 especially at low temperatures, they were largely unselective and resulting in the formation of NO_x (Fig. S8). On the contrary, the Fe/ZSM-5 (T_{50} = 255 °C) despite being less active, show comparable selectivity as the Cu/ZSM-5. The Ag/ZSM-5 displayed the lowest activity (T_{50} = 358 °C) almost matching that of the H/ZSM-5 (Fig. S8).

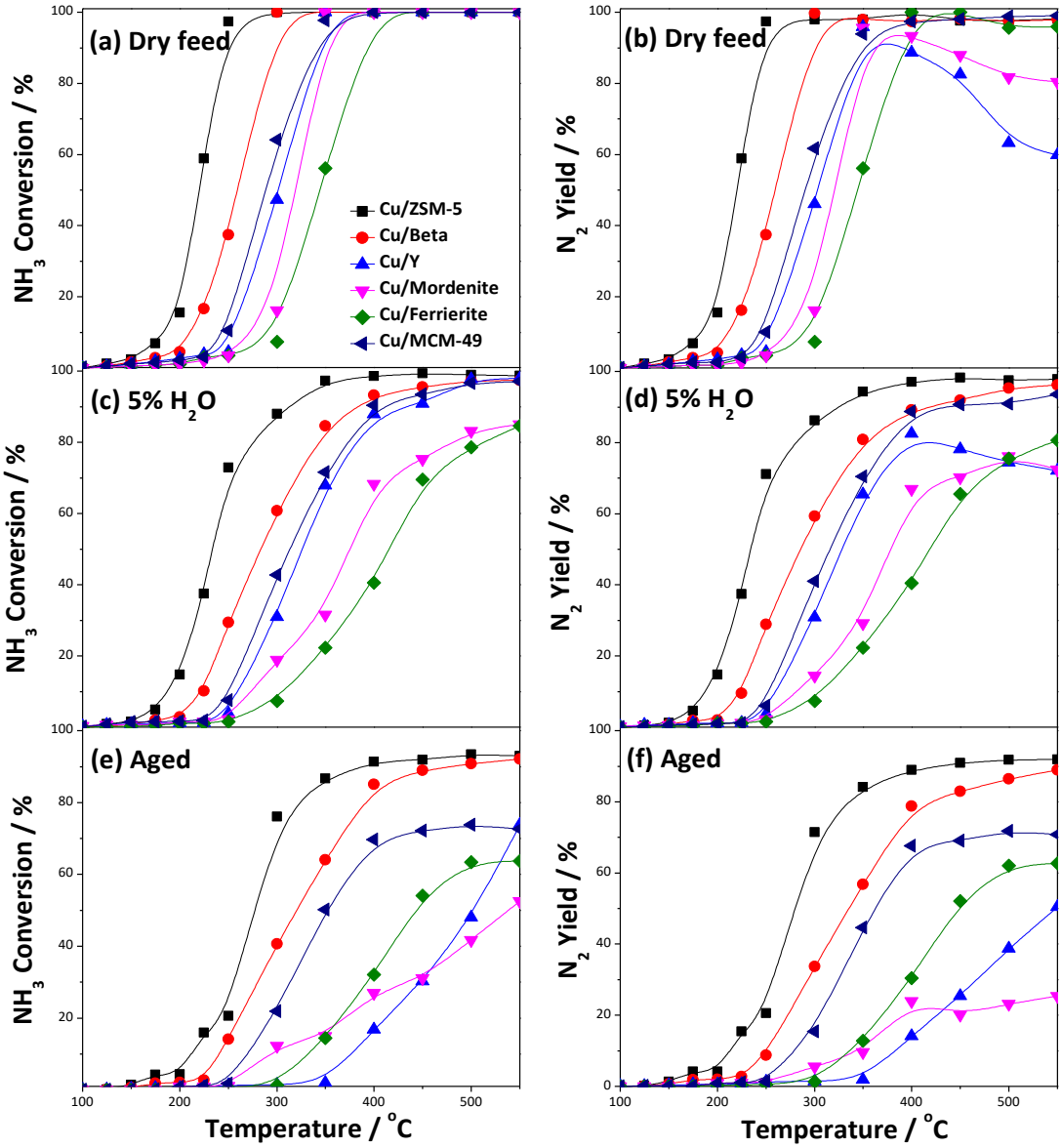

Fig. 6. Catalytic NH_3-SCO conversion and the corresponding N_2 yield of different Cu/zeolites (a,b) under dry feed, and (c,d) in the addition of 5% H_2O in the feed stream. (e,f) The performance of the hydrothermally aged (850 °C, 8 h in 5% H_2O/air) Cu/zeolites assessed under the same condition as (e,f). Reactant feed: 1000 ppm NH_3, 10% O_2, with or without 5% H_2O, the rest in He, GHSV = 45,000 h^{-1}.

For a more practical assessment of the Cu/zeolites, 5% H_2O was introduced into the reactant feed gas. As shown in Fig. 6c,d, the presence of moisture affected the NH_3-SCO activity of the Cu/zeolites to different extent while maintaining the same activity trend as that

in the dry feed. The nano Cu/ZSM-5 (T_{50} = 230 °C), Cu/Beta (T_{50} = 280 °C), Cu/MCM-49 (T_{50} = 315 °C), Cu/Y (T_{50} = 330 °C) were only moderately affected by the additional moisture. By comparison, the Cu/Mordenite (T_{50} = 375 °C) and Cu/Ferrierite (T_{50} = 415 °C) were more sensitive, resulting in < 85% NH_3 conversion even at up to 550 °C. The presence of H_2O is known to compete with the NH_3 for the adsorption on active sites,[49] while the resultant formation of nitrates may further block the active sites and cause dealumination.[50,51] Further assessments were carried out on the aged Cu/zeolites that were hydrothermally treated at 850 °C for 8 h in the presence of 5% H_2O (Fig. 6e, f). Despite some deactivation after the hydrothermal aging, the nano Cu/ZSM-5 (T_{50} = 260 °C) and Cu/Beta (T_{50} = 308 °C) continue to exhibit good NH_3-SCO activities with N_2 yield above 85%. The former is particularly impressive in maintaining most of the crystallinity (Fig. 7a) and micropore structures (Fig. 7b) as well as SSA (275 m^2 g^{-1}). Only some minor extent of phase transformation was observed for Cu/Beta by forming crystalline $AlSi_2O_6(OH)_2$ and $Al_{22}Si_8O_{49}\cdot 22H_2O$ (Fig. 7a), accompanied by some losses in micropore volume (Fig. 7b) and SSA (270 m^2 g^{-1}). As shown in Table 4, the Cu dispersions for nano Cu/ZSM-5 and Cu/Beta were decreased from 82 to 51% and from 76 to 46%, respectively, after the hydrothermal aging. The Cu/MCM-49 experienced a significant loss in Cu dispersion from 73 to 23% due to the formation of crystalline $Cu(OH)_2\cdot H_2O$ (from the aggregation of dispersed Cu). As a result, a low N_2 yield ~70% was measured. By comparison, the other Cu/zeolites, namely Cu/Y, Cu/Mordenite, and Cu/Ferrierite experienced more severe deactivation related to the mixed formation of aluminium silicates and $Cu(OH)_2\cdot H_2O$, as well as severe loss of SSAs (Table 4). The Cu dispersions were 15, 9 and 10%, respectively (Table 4). In the case of Cu/Mordenite, the complete loss of the zeolite crystallinity (i.e., amorphization, Fig. 8a) as well as its pore structure (Fig. 7b) resulted in the lowest NH_3-SCO activity and maximum N_2 yield of only 22%. Essentially, the measured performance of the aged Cu/Mordenite was that of a non-porous catalyst consisting of mildly active $Cu(OH)_2\cdot H_2O$ deposits. The results highlight the utmost challenge in preserving both the structure rigidity of the zeolite and the dispersion of the active Cu species under hydrothermal conditions, where the Cu/ZSM-5 and to a certain degree Cu/Beta, show credible potentials as practical NH3-SCO catalysts.

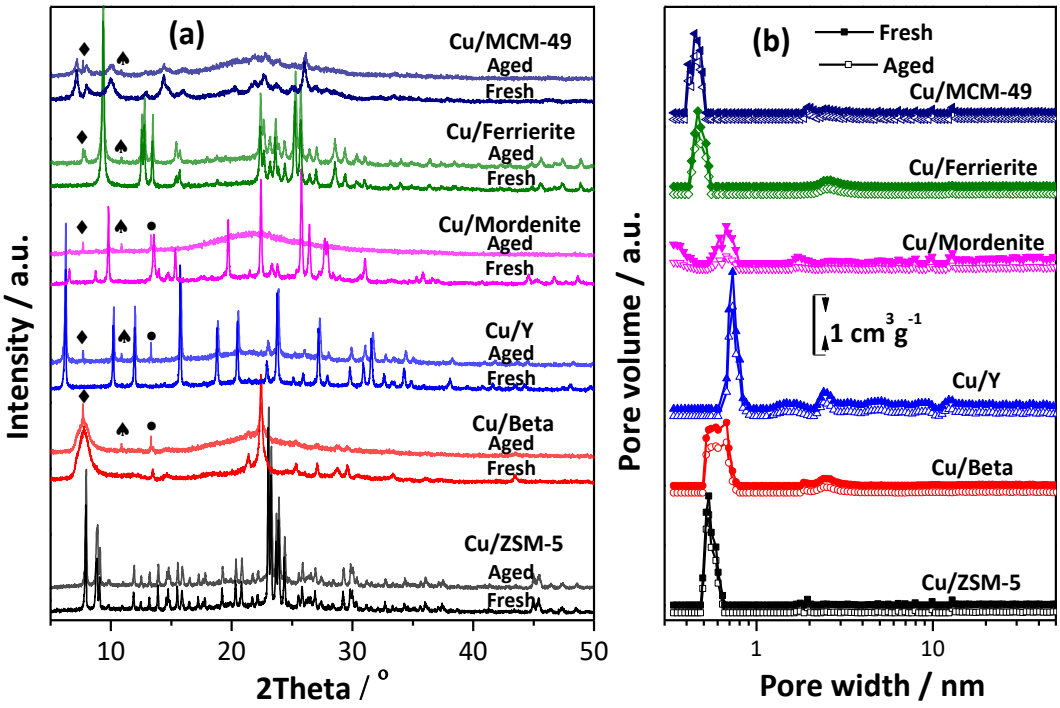

Fig. 7. The (a) XRD and (b) pore size distribution of the as-prepared Cu/zeolites and that after hydrothermal aging (850 °C, 8 h in 5% H_2O/air). While the diffraction peaks of the as-prepared fresh samples in (a) correspond to that of the pristine zeolites, the additional peaks after hydrothermal treatment are identified as aluminium silicate hydroxide, $AlSi_2O_6(OH)_2$ (♦ symbol, ICSD: 00-002-0037), aluminium silicate oxide hydrate, $Al_{22}Si_8O_{49}\cdot 22H_2O$ (♠ symbol, ICSD: 00-011-0378), and $Cu(OH)_2\cdot H_2O$ (● symbol, ICSD: 00-42-0638).

Table 4. Cu dispersions on the fresh and hydrothermally aged (850 °C, 8 h in 5% H_2O/air) Cu/zeolites, as well as the specific surface area (SSA) and isolated Cu^{2+} compositions of the latter.

Catalyst	Dispersion, Fresh catalyst (%)	Dispersion, Aged catalyst (%)	SSA, Aged catalyst ($m^2\ g^{-1}$)	Cu^{2+} composition, Aged catalyst ($\mu mol\ g^{-1}$)[a]
Cu/ZSM-5	82	51	285	298
Cu/Beta	76	46	280	257
Cu/Y	73	15	298	222
Cu/Mordenite	71	9	48	56
Cu/Ferrierite	51	10	126	196
Cu/MCM-49	73	23	192	210

[a] Calculated based on the H_2-TPR (Fig. S6)

The apparent activation energies (E_a) of the NH_3-SCO were deduced from the Arrhenius plots. Fig. 8 compares the corresponding plots for the Cu/zeolites measured in the absence or presence of 5% H_2O in the feed gas, as well as that after hydrothermal aging. As further shown in Fig. 8d, the extracted E_a for the Cu/zeolites, in the exception of Cu/MCM-49 (E_a = 47±7 kJ mol^{-1}), was found to be 71±8 kJ mol^{-1} when assessed using dry feed. Despite the lower activity with the addition of 5% H_2O, the E_a hardly changed (43±7 kJ mol^{-1} for Cu/MCM-49, 65±7 kJ mol^{-1} for all other Cu/zeolites) suggesting that the presence of moisture may have blocked some of the active sites leading to the slightly lower NH_3-SCO activity but it did not significantly alter the reaction pathway. The anomalous reaction mechanism for Cu/MCM-49 will be clarified in more details using the *in situ* DRIFTS (next section). Upon hydrothermal aging, the E_a of Cu/MCM-49 increased to 72±7 kJ mol^{-1}, consistent with the rest of the Cu/zeolite catalysts (68±8 kJ mol^{-1}), which is in turn comparable to those of the fresh catalysts. This is true despite the severe loss of Cu dispersion and SSA for many of the Cu/zeolites after the harsh hydrothermal aging seen above. The result again points to the decreased activity due to the loss of active sites, but the reaction mechanism is largely maintained.

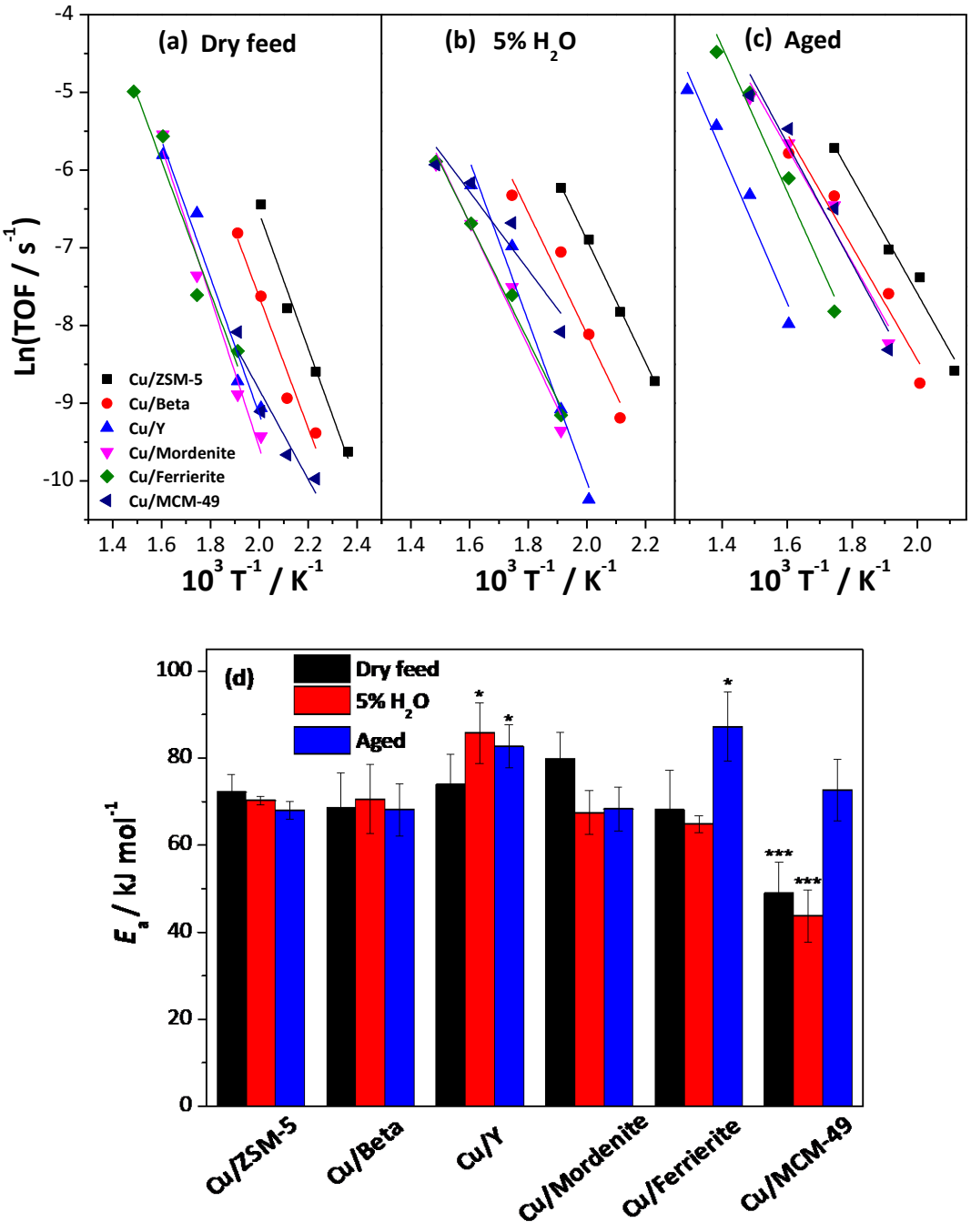

Fig. 8. The Arrhenius plots of Cu/zeolites assessed under (a) dry feed, (b) in the addition of 5% H_2O in the feed stream, as well as that (c) after hydrothermal aging. (d) The corresponding apparent active energies measured for the three conditions above. The TOF was calculated by normalizing to the Cu dispersion measured for (a,b) fresh and (c) aged catalysts. Reactant feed: 1000 ppm NH_3, 10% O_2, with or without 10% H_2O, the rest in He, GHSV = 45,000 h^{-1}.

3.3. *In situ* DRIFTS and NH_3-SCO mechanisms on Cu/zeolites

The *in situ* DRIFTS was further used to probe the surface speciation of the intermediates. To do so, we first monitored the surface adsorption of 500 ppm NH_3/He on the Cu/zeolites surface where various adsorbed intermediate species were formed (Fig. 9). This was followed by the introduction of 10% O_2/He to initiate the NH_3-SCO reaction with the adsorbed NH_3 intermediates (Fig. 10). By monitoring the new intermediate species that were formed during the NH_3-SCO reaction, this provides a glimpse on the possible reaction mechanism specific to each Cu/zeolite catalyst.

Fig. 9 shows the DRIFT spectra of NH_3 adsorption on the different topological Cu/zeolites at different temperatures. The peaks intensity decreased with the increasing temperature as a result of higher desorption equilibrium. In general, several bands at 1458, 1505, 1558, 1640, 1692, 3200, 3295, 3400, 3606, 3630, 3680 and 3750 cm^{-1} were observed across different Cu/zeolites. The bands at 1458 cm^{-1} and 1692 cm^{-1} were attributed to the asymmetric and symmetric deformation modes of adsorbed NH_3 on Brønsted acid sites (NH_4^+), respectively.[52] The coordinated NH_3 adsorbed on Lewis acid sites were reflected by the bands at 1640 cm^{-1} and 3330 cm^{-1}.[53] Seven bands assigned to the N-H telescopic vibrations were observed in the range of 3100-3500 cm^{-1}. Among them, the band at 3200 cm^{-1} is related to NH_3 adsorbed on Cu^{2+} sites,[54] appearing on Cu/ZSM-5, Cu/Beta and Cu/Ferrierite zeolites (Fig. 9a, b, e). Correspondingly, the bands at 3275, 3295, 3330, 3350, 3370 and 3400 cm^{-1} were attributed to NH_4^+ group.[55] Meanwhile, the negative bands at 3584, 3606, 3630, 3680, 3700, 3740, 3750, and 3790 cm^{-1} were assigned to the surface O–H vibrations.[53,54] It is worth noting that the band at 3653 cm^{-1} only appeared on Cu/ZSM-5 and Cu/Y (Fig. 9a, c) belonging to the ν(OH) stretching of $[Cu_2^+(OH)^-]^+$ species. The other bands were related to the NH_3 chemisorption on Si–OH–Al acid sites,[50] which exhibits dynamic characteristics with the increase in temperature. For example, the 3680 cm^{-1} band on Cu/ZSM-5 initially increased up to 200 °C and then decreased at higher temperatures, indicating that a lot of NH_3 reacted with the acid sites to form amide ($–NH_2$) below 200 °C. This is substantiated by the enhancement in the amide band at

1558 cm^{-1}. The bands belonging to monodentate (1505, 1510 and 1544 cm^{-1}) and bidentate nitrates (1570 cm^{-1}) were also observed on Cu/ZSM-5, Cu/Beta, Cu/Y and Cu/Mordenite as a result of the oxidative NH_3 adsorption.

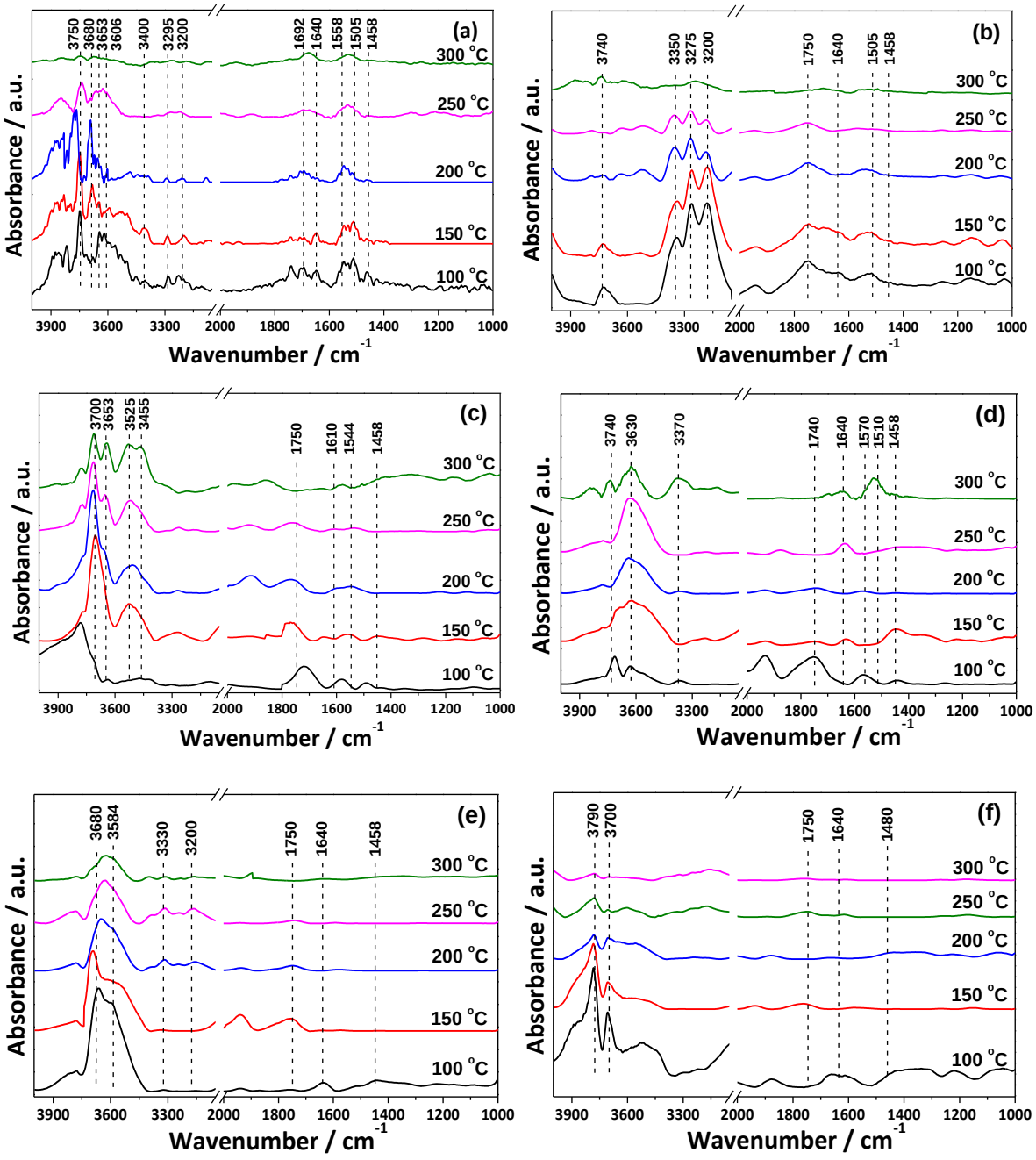

Fig. 9. *In situ* DRIFTS spectra of (a) Cu/ZSM-5, (b) Cu/Beta, (c) Cu/Y, (d) Cu/Mordenite, (e) Cu/Ferrierite and (f) Cu/MCM-49 catalyst treated with a flow of 500 ppm NH_3/He at various temperatures.

To investigate the mechanism of NH_3-SCO, the NH_3-saturated Cu/zeolites were purged with He and followed by the introduction of 10% O_2/He at 200 °C. As shown from the DRIFTS of the three most active catalysts, i.e., Cu/ZSM-5, Cu/Beta and Cu/MCM-49, the bands attributed to the NH_3 adsorbed on Brønsted (1458 cm^{-1}) and Lewis acid sites (1640 cm^{-1}) decreased with the increase in O_2 exposure and nearly vanished after 30 min due to the NH_3-SCO reaction (Fig. 10). In particular of Cu/ZSM-5 (Fig. 10a) and Cu/Beta (Fig. 10b), the bands of N–H vibration (3275, 3295, 3350, and 3400 cm^{-1}) gradually decreased while the bands of amide (1558 cm^{-1}) and nitrates (1505 cm^{-1}) increased slightly and then decreased, indicating that NH_4^+ ad-species were activated and reacted with O_2 to form $–NH_2$ and nitrate intermediates. The bands for N–H (3275 cm^{-1}) and $–NH_2$ (1523 cm^{-1}) gradually increased in the case of Cu/MCM-49 (Fig. 10f). It is worth noting that the HNO bands at 1480 cm^{-1} and 1875 cm^{-1},[56] which are unique to Cu/MCM-49, increased gradually over time. No characteristic bands of $–NH_2$ was observed for the Cu/Y, Cu/Mordenite and Cu/Ferrierite catalysts (Fig. 10c-e), but the bands at 1740 and 1750 cm^{-1} related to N_2O_4 could be measured,[54] confirming the formation of NO_x species.[56] Similarly, the band at 1580 cm^{-1} in Cu/Y, Cu/Mordenite and Cu/Ferrierite is assigned to NO_x and predominantly NO in this case.

Imide mechanism route:

$NH_3 \rightarrow NH_2 + H$ (Eq. 2)

$NH_2 \rightarrow NH + H$ (Eq. 3)

$NH + O \rightarrow HNO$ (Eq. 4)

$NH + HNO \rightarrow N_2 + H_2O$ (Eq. 5)

$2HNO \rightarrow N_2O + H_2O$ (Eq. 6)

iSCR mechanism route:

$O_2 \rightarrow 2O$ (Eq. 7)

$NH_3 + O \rightarrow NH + H_2O$ (Eq. 8)

$NH + O_2 \rightarrow NO + OH$ (Eq. 9)

$NH_2 + NO \rightarrow NH_2NO \rightarrow N_2 + H_2O$ (Eq. 10)

$NO + NH_3 + O_2 \rightarrow N_2O + H_2O$ (Eq. 11)

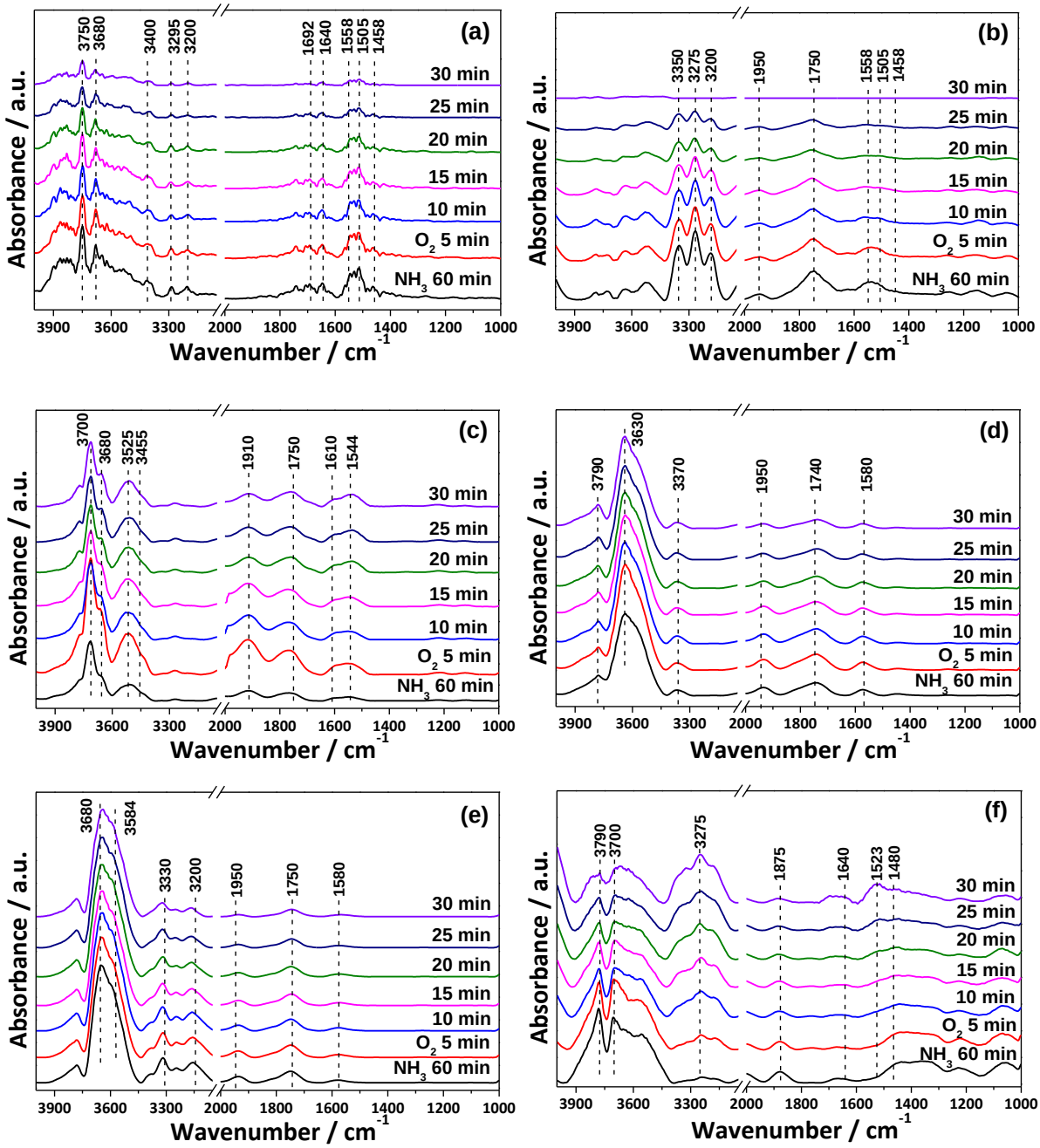

Fig. 10. *In situ* DRIFTS at 200 °C upon passing 10% O_2/He over the NH_3 pre-adsorbed on (a) Cu/ZSM-5, (b) Cu/Beta, (c) Cu/Y, (d) Cu/Mordenite, (e) Cu/Ferrierite, (f) Cu/MCM-49 catalysts for 0, 5, 10, 15, 20, 25 and 30 min.

Based on the studies above, it can summarized that $-NH_2$ species (1523 and 1558 cm^{-1}), nitrates species (1505 cm^{-1}), N_2O_4 (1740, 1750 cm^{-1}) and NH_4^+ (3200, 3275 cm^{-1}) could be observed on all Cu/zeolites. In addition, HNO (1480 cm^{-1}) species only occurred on the Cu/MCM-49 zeolite, likely on the unique $Cu(H_2O)$ complex sites in the vicinity of the framework oxygen (as probed by EPR). The speciation on Cu/MCM-49 appears to be consistent with the imide mechanism (Eq. 2-6), while reaction on the other Cu/zeolites might take place via the iSCR mechanism (Eq. 7-11). Previous report has indicated that the imide mechanism preferentially occurs at low temperature, while the iSCR mechanism dominates at higher temperatures.[57] The observation further infers that the imide mechanism is defined by the lower energy barrier than the iSCR mechanism, which is consistent with the lowest E_a measured for Cu/MCM-49 as compared with other Cu/zeolites. Since the kinetic diameters of the largest intermediate species, i.e., HNO (3.17 Å) for imide mechanism and NH_2NO (3.81 Å) for iSCR mechanism, are significantly smaller than the physical pore dimension (Figure S9), we envision that larger transition state molecule(s) closer to the dimensions of the 10-MR channel or the intersection pores may exist to benefit from the steric confinement effect for achieving high N_2 selectivity.

4. Conclusions

The work successfully demonstrated a new series of highly active Cu/zeolites (Si/Al = 10-15) for the selective NH_3-SCO reaction. The catalytic activity (based on T_{50}) follows the order of nano Cu/ZSM-5 > Cu/Beta > Cu/MCM-49 > Cu/Y > Cu/Mordenite > Cu/Ferrierite, with half conversion recorded at temperature as low as 220 °C. The isolated Cu^{2+} and Cu^+ were identified as the highly active sites, while surface CuO although less active, also contributed (albeit mildly) to the NH_3-SCO conversions. Cu/zeolites with small channel pores, i.e., Cu/ZSM-5, Cu/Beta, Cu/MCM-49 and Cu/Ferrierite, were favorable in maintaining high N_2 selectivity (yield > 95%) even at temperatures as high as 500 °C, while the larger pore Cu/zeolites (Cu/Y and Cu/Mordenite) started to produce NO_x at 400 °C and above. While the activity was mildly decreased when assessed in the presence of moisture addition to the feed

stream, and further decreased when using hydrothermally aged catalysts, the activity trend of the Cu/zeolites remains the same. When using fresh catalysts, a significantly lower apparent activation energy was measured for Cu/MCM-49 compared with other Cu/zeolites. Observations under *in situ* DRIFTS suggested the occurrence of iSCR and imide mechanisms, respectively. However, upon hydrothermal aging, all Cu/zeolites recorded similar activation energies specific to the imide mechanism. To the best of our knowledge, the work is the first to show the critical importance of the combination of the amount of isolated Cu ions and micropore topologies (10-MR channel pores) in ensuring high SCO-NH_3 activity and N_2 selectivity. Importantly, the work demonstrates the good performance of the Cu/zeolites especially that nano Cu/ZSM-5 under practical conditions, i.e., in the presence of moisture and after hydrothermal aging. The insights gained from the current work shall pave the way for the exploration of other active NH_3-SCO catalysts based on isolated metal cations supported on zeolites.

Conflicts of interest

The authors declare no competing financial interest.

Acknowledgements

The financial supports of the National Natural Science Foundation of China (No. U1862102), and the Fundamental Research Funds for the Central Universities (XK1802-1, JD1903) are gratefully acknowledged.

Supplementary material

More information on the XRD of H/zeolites, SEM, NH_3-TPD, NH_3-SCO of CuO, as well as the byproducts yields among different zeolites with dry feed, 5% H_2O and after hydrothermal treatment are available in the Supporting Information. In addition, the active test of different Si/Al ratio Cu/ZSM-5, different noble-metal and transition metal modified ZSM-5 is also

available in the Supporting Information.

Notes and references

1 X. Chen, P. Wang, P. Fang, H. Wang, C. Cen, W. Zeng, Z. Wu, Design strategies for SCR catalysts with improved N_2 selectivity: the significance of nano-confining effects by titanate nanotubes, *Environ. Sci.: Nano*, 2017, **4,** 437–447.

2 Y. Cheng, J. Liu, Z. Zhao, Y. Wei, W. Song, C. Xu, The simultaneous purification of PM and NO_x in diesel engine exhausts over a single 3DOM $Ce_{0.9-x}Fe_{0.1}Zr_xO_2$ catalyst, *Environ. Sci.: Nano*, 2017, **4,** 1168–1177.

3 W. Yang, Q. Ma, Y. Liu, J. Ma, B. Chu, H. He, The effect of water on the heterogeneous reactions of SO_2 and NH_3 on the surfaces of α-Fe_2O_3 and γ-Al_2O_3, *Environ. Sci.: Nano*, 2019, **6,** 2749–2758.

4 X. Cui, J. Zhou, Z. Ye, H. Chen, L. Li, M. Ruan, J. Shi, Selective catalytic oxidation of ammonia to nitrogen over mesoporous CuO/RuO_2 synthesized by co-nanocasting-replication method, *J. Catal.*, 2010, **270,** 310–317.

5 D. Wang, Y. Peng, Q. Yang, Performance of modified $La_xSr_{1-x}MnO_3$ perovskite catalysts for NH_3 oxidation: TPD, DFT, and Kinetic studies, *Environ. Sci. Technol.*, 2018, **52,** 7443–7449.

6 J. Gong, R. A. Ojifinni, T. S. Kim, J. M. White, C. B. Mullins, Selective catalytic oxidation of ammonia to nitrogen on atomic oxygen precovered Au(111), *J. Am. Chem. Soc.*, 2006, **128,** 9012–9013.

7 J. Zhu, J. Wang, J. Wang, L. Lv, X. Wang, M. Shen, New insights into the N_2O formation mechanism over Pt-BaO/Al_2O_3 model catalysts using H_2 as a reductant, *Environ. Sci. Technol.*, 2015, **49,** 504–512.

8 Y. Katayama, T. Okanishi, H. Muroyama, T. Matsui, K. Eguchi, Enhancement of ammonia oxidation activity over Y_2O_3-modified platinum surface: Promotion of $NH_{2,ad}$ dimerization process, *J. Catal.*, 2016, **344,** 496–506.

9 M. Yang, C. Wu, C. Zhang, H. He, Selective oxidation of ammonia over copper-silver-based catalysts, *Catal. Today*, 2004, **90,** 263–267.

10 T. Curtin, F. O'Regan, C. Deconinck, N. Knüttle, B. K. Hodnett, The catalytic oxidation of ammonia: influence of water and sulfur on selectivity to nitrogen over promoted copper oxide/alumina catalysts, *Catal. Today*, 2000, **55,** 189–195.

11 L. Gang, J. van Grondelle, B. G. Anderson, R. A. van Santen, Selective low temperature NH_3 oxidation to N_2 on copper-based catalysts, *J. Catal.*, 1999, **186,** 100–109.

12 L. Chmielarz, M. Jabłońska, A. Strumiński, Z. Piwowarska, A. Węgrzyn, S. Witkowski, M. Michalik, Selective catalytic oxidation of ammonia to nitrogen over Mg-Al, Cu-Mg-Al and Fe-Mg-Al mixed metal oxides doped with noble metals, *Appl. Catal. B*, 2013, **130–131,** 152–162.

13 C. Liang, X. Li, Z. Qu, M. Tade, S. Liu, The role of copper species on Cu/γ-Al_2O_3 catalysts for NH_3-SCO reaction, *Appl. Surf. Sci.*, 2012, **258,** 3738–3743.

14 R. Q. Long, R. T. Yang, Selective catalytic oxidation (SCO) of ammonia to nitrogen over Fe-exchanged zeolites, *J. Catal.*, 2001, **201,** 145–152.

15 G. Qi, J. E. Gatt, R. T. Yang, Selective catalytic oxidation (SCO) of ammonia to nitrogen over Fe-exchanged zeolites prepared by sublimation of $FeCl_3$, *J. Catal.*, 2004, **226,** 120–128.

16 Z. Wang, Z. Qu, X. Quan, Z. Li, H. Wang, R. Fan, Selective catalytic oxidation of ammonia to nitrogen over CuO-CeO_2 mixed oxides prepared by surfactant-templated method, *Appl. Catal. B*, 2013, **134–135,** 153–166.

17 R. Q. Long, R. T. Yang, Superior ion-exchanged ZSM-5 catalysts for selective catalytic oxidation of ammonia to nitrogen, *Chem. Commun.*, 2000, **17,** 1651–1652.

18 M. Jabłońska, A. Król, E. K. Zajac, K. Tarach, L. Chmielarz, K. G. Marek, Zeolite Y modified with palladium as effective catalyst for selective catalytic oxidation of ammonia to nitrogen, *J. Catal.*, 2014, **316,** 36–46.

19 Z. Qu, H. Wang, S. Wang, H. Cheng, Y. Qin, Z. Wang, Role of the support on the behavior of Ag-based catalysts for NH_3 selective catalytic oxidation (NH_3-SCO), *Appl. Surf. Sci.*, 2014, **316,** 373–379.

20 N. I. Il'chenko, Catalytic oxidation of ammonia, Russ. *Chem. Rev.*, 1976, **45,** 1119–1134.

21 G. Qi, R. T. Yang, Selective catalytic oxidation (SCO) of ammonia to nitrogen over Fe/ZSM-5 catalysts, *Appl. Catal. A*, 2005, **287,** 25–33.

22 R. Zhang, W. Y. Teoh, R. Amal, B. Chen, S. Kaliaguine, Catalytic reduction of NO by CO over $Cu/Ce_xZr_{1-x}O_2$ prepared by flame synthesis, *J. Catal.*, 2010, **272,** 210–219.

23 Y. Zhang, C. Li, C. Yu, T. Tran, F. Guo, Y. Yang, J. Yu, G. Xu, Synthesis, characterization and activity evaluation of Cu-based catalysts derived from layered double hydroxides (LDHs) for $DeNO_x$ reaction, *Chem. Eng. J.*, 2017, **330,** 1082–1090.

24 X. W. Cheng, J. Wang, J. Guo, H. He, Y. Long, FER zeolite crystallized in THF-Na_2O-SiO_2-Al_2O_3-H_2O reactant system containing catalytic amount of organic additives, *Microporous Mesoporous Mater.*, 2009, **119,** 60–67.

25 K. Hayasaka, D. Liang, W. Huybrechts, B. R. De Waele, K. J. Houthoofd, P. Eloy, E. M. Gaigneaux, G. van Tendeloo, J. W. Thybaut, G. B. Marin, Formation of ZSM-22 zeolite catalytic particles by fusion of elementary nanorods, *Chem.- Eur. J.*, 2007, **13,** 10070–10077.

26 M. Iijima, W. A. Brantley, N. Baba, S. B. Alapati, T. Yuasa, H. Ohno, I. Mizoguchi, Micro-XRD study of beta–titanium wires and infrared soldered joints, *Dent. Mater.*, 2007, **23,** 1051–1056.

27 G. von Willingh, H. S. Abbo, S. J. J. Titinchi, Selective oxidation reactions over tri- and tetradentate oxovanadium(IV) complexes encapsulated in zeolite-Y, *Catal. Today*, 2014, **227,** 96–104.

28 B. Xu, H. Li, W. Hua, Y. Yue, Z. Gao, Role of surface pockets on MCM-49 structure in the alkylation of hydroquinone with tert-butanol, *J. Catal.*, 2006, **240,** 31–38.

29 R. Zhang, N. Liu, Z. Lei, B. Chen, Selective transformation of various nitrogen-containing exhaust gases toward N_2 over zeolite catalysts, *Chem. Rev.*, 2016, **116,** 3658–3721.

30 M. Occhiuzzi, G. Fierro, G. Ferraris, G. Moretti, Unusual complete reduction of Cu^{2+} species in Cu-ZSM-5 zeolites under vacuum treatment at high temperature, *Chem. Mater.*, 2012, **24,** 2022−2031.

31 J. Park, H. J. Park, J. H. Baik, I. S. Nam, C. H. Shin, J. H. Lee, B. K. Cho, S. H. Oh, Hydrothermal stability of Cu-ZSM5 catalyst in reducing NO by NH_3 for the urea selective catalytic reduction process, *J. Catal.*, 2006, **240,** 47–57.

32 R. Kydd, W. Y. Teoh, K. Wong, Y. Wang, J. Scott, Q. H. Zeng, A. B. Yu, J. Zou, R. Amal, Flame-synthesized ceria-supported copper dimers for preferential oxidation of CO, *Adv. Funct. Mater.*, 2009, **19,** 369–377.

33 F. Gao, E. D. Walter, E. M. Karp, J. Luo, R. G. Tonkyn, J. H. Kwak, J. Szanyi, C. H. F. Peden, Structure-activity relationships in NH_3-SCR over Cu-SSZ-13 as probed by reaction kinetics and EPR studies, *J. Catal.*, 2013, **300,** 20–29.

34 T. Nanba, S. Masukawa, A. Ogata, J. Uchisawa, A. Obuchi, Active sites of Cu-ZSM-5 for the decomposition of acrylonitrile, *Appl. Catal. B*, 2005, **61,** 288–296.

35 A. Sultana, T. Nanba, M. Sasaki, M. Haneda, K. Suzuki, H. Hamada, Selective catalytic reduction of NO_x with NH_3 over different copper exchanged zeolites in the presence of decane, *Catal. Today*, 2011, **164,** 495–499.

36 B. E. R. Snyder, M. L. Bols, R. A. Schoonheydt, B. F. Sels, E. I. Solomon, Iron and copper active sites in zeolites and their correlation to metalloenzymes, *Chem. Rev.*, 2018, **118,** 2718−2768.

37 F. Giordanino, P. N. R. Vennestrøm, L. F. Lundegaard, F. N. Stappen, S. Mossin, P. Beato, S. Bordigaa, C. Lamberti, Characterization of Cu-exchanged SSZ-13: a comparative FTIR, UV-Vis, and EPR study with Cu-ZSM-5 and Cu-β with similar Si/Al and Cu/Al ratios, *Dalton Trans.*, 2013, **42,** 12741−12761.

38 Y. J. Kim, J. K. Lee, K. M. Min, S. B. Hong, I. S. Nam, B. K. Cho, Hydrothermal stability of Cu-SSZ13 for reducing NO_x by NH_3, *J. Catal.*, 2014, **311,** 447–457.

39 A. De Lucas, J. L. Valverde, F. Dorado, A. Romero, I. Asencio, Influence of the ion exchanged metal (Cu, Co, Ni and Mn) on the selective catalytic reduction of NO_x over mordenite and ZSM-5, *J. Mol. Catal. A*, 2005, **225,** 47–58.

40 D. L. Hoang, T. T. H. Dang, J. Engeldinger, M. Schneider, J. Radnik, M. Richter, A. Martin, TPR investigations on the reducibility of Cu supported on Al_2O_3, zeolite Y and SAPO-5, *J. Solid State Chem.*, 2011, **184,** 1915–1923.

41 C. Torre-Abreu, M. F. Ribeiro, C. Henriques, G. Delahay, NO TPD and H_2-TPR studies for characterisation of Cu-MOR catalysts The role of Si/Al ratio, copper content and cocation, *Appl. Catal. B*, 1997, **14,** 261–272.

42 M. Richter, M. J. G. Fait, R. Eckelt, E. Schreier, M. Schneider, M. M. Pohl, R. Fricke, Oxidative gas phase carbonylation of methanol to dimethyl carbonate over chloride-free Cu-impregnated zeolite Y catalysts at elevated pressure, *Appl. Catal. B*, 2007, **73,** 269–281.

43 R. Kefirov, A. Penkova, K. Hadjiivanov, S. Dzwigaj, M. Che, Stabilization of Cu^+ ions in BEA zeolite: Study by FTIR spectroscopy of adsorbed CO and TPR, *Microporous Mesoporous Mater.*, 2008, **116,** 180–187.

44 A. C. Akah, G. Nkeng, A. A. Garforth, The role of Al and strong acidity in the selective catalytic oxidation of NH_3 over Fe-ZSM-5, *Appl. Catal. B*, 2007, **74,** 34–39.

45 E. Borfecchia, P. Beato, S. Svelle, U. Olsbye, C. Lamberti cd, S. Bordiga, Cu-CHA – a model system for applied selective redox catalysis, *Chem. Soc. Rev.*, 2018, **47,** 8097–9133.

46 A. Flura, F. Can, X. Courtois, S. Royer, D. Duprez, High-surface-area zinc aluminate supported silver catalysts for low-temperature SCR of NO with ethanol, *Appl. Catal. B*, 2012, **126,** 275–289.

47 N. Panahi, Parvaneh, Comparative study of ZSM-5 supported transition metal (Cu, Mn, Co, and Fe) nanocatalysts in the selective catalytic reduction of NO with NH_3, *Environ. Prog. Sustain. Energy*, 2017, **4,** 1049–1055.

48 N. Liu, R. Zhang, B. Chen, Y. Li, Y. Li, Comparative study on the direct decomposition of nitrous oxide over M (Fe, Co, Cu)–BEA zeolites, *J. Catal.*, 2012, **294,** 99–112.

49 T. Zhang, H. Chang, Y. You, C. Shi, J. Li, Excellent activity and selectivity of one-pot synthesized Cu-SSZ-13 catalyst in the selective catalytic oxidation of ammonia to nitrogen, *Environ. Sci. Technol.*, 2018, **52,** 4802−4808.

50 A. Kowalczyk, A. Święs, B. Gila, M. Rutkowska, Z. Piwowarska, A. Borcuch, M. Michalik, L. Chmielar, Effective catalysts for the low-temperature NH_3-SCR process based on MCM-41 modified with copper by template ion-exchange (TIE) method, *Appl. Catal. B*, 2018, **237,** 927–937.

51 K. Zha, L. Kang, C. Feng, L. Han, H. Li, T. Yan, P. Maitarad, L. Shi, D. Zhang, Improved NO_x reduction in the presence of alkali metals by using hollandite Mn–Ti oxide promoted Cu-SAPO-34 catalysts, *Environ. Sci.: Nano*, 2018, **5,** 1408–1419.

52 L. Zhang, H. He, Mechanism of selective catalytic oxidation of ammonia to nitrogen over Ag/Al_2O_3, *J. Catal.*, 2009, **268,** 18–25.

53 L. Xie, F. Liu, K. Liu, X. Shi, H. He, Inhibitory effect of NO_2 on the selective catalytic reduction of NO_x with NH_3 over one-pot-synthesized Cu-SSZ-13 catalyst, *Catal. Sci. Technol.*, 2014, **4,** 1104–1110.

54 D. Wang, L. Zhang, K. Kamasamudram, W. S. Epling, In situ-DRIFTS study of selective catalytic reduction of NO_x by NH_3 over Cu-exchanged SAPO-34, *ACS Catal.*, 2013, **3,** 871–881.

55 R. Zhang, B. Zhang, Z. Shi, N. Liu, B. Chen, Catalytic behaviors of chloromethane combustion over the metal-modified ZSM-5 zeolites with diverse SiO_2/Al_2O_3 ratios, *J. Mol. Catal. A*, 2015, **398,** 223–230.

56 K. I. Hadjiivanov, Identification of neutral and charged N_xO_y surface species by IR spectroscopy, *Catal. Rev.*, 2000, **42,** 71–144.

57 W. Chen, Z. Qu, W. Huang, X. Hu, N. Yan, Novel effect of SO_2 on selective catalytic oxidation of slip ammonia from coal-fired flue gas over IrO_2 modified Ce-Zr solid solution and the mechanism investigation, *Fuel*, 2016, **166,** 179–187.